Original Paper

phys. stat. sol. (b) **243**, No. 9, 2133–2150 (2006) / **DOI** 10.1002/pssb.200666817

Theory of spintronic materials

James R. Chelikowsky[*, 1], **Efthimios Kaxiras**[2], and **Renata M. Wentzcovitch**[3]

[1] Center for Computational Materials, Institute for Computational Engineering and Sciences, Departments of Physics and Chemical Engineering, University of Texas, Austin, TX 78712, USA
[2] Department of Physics and Division of Engineering and Applied Sciences, Harvard University, Cambridge, MA 02138, USA
[3] Department of Chemical Engineering and Materials Science, and the Minnesota Supercomputing Institute, University of Minnesota, Minneapolis, MN 55455, USA

Received 13 April 2006, accepted 1 May 2006
Published online 10 July 2006

PACS 72.25.Dc, 85.75.–d

The ability to manipulate and understand spin polarized materials is a key to constructing spintronic devices, i.e., devices in which the electron's *spin* and charge are both utilized. Here we review computational methods for predicting the properties of spin-polarized materials at the macro- and nano-limits, and at interfaces.

© 2006 WILEY-VCH Verlag GmbH & Co. KGaA, Weinheim

1 Introduction

Magnetic devices serve as the basis for information processing and storage. In particular, magnetism in metals has been the backbone of information storage for years. A key event in this area was the discovery in 1988 of the giant magneto-resistance (GMR) effect, where the resistance of a thin-film ferromagnetic/nonmagnetic layer sandwich is strongly magnetic field dependent. The GMR effect is now at the heart of almost every modern computer hard drive. Further advances in this area may come from other types of magnetic devices: devices which manipulate both the *spin* and the *charge* of the electron. These so called "spintronic" devices may lead to more exotic information devices, capable of a wide variety of functionality [1–4]. Two notable examples of proposed spintronic devices are the "spin field effect transistor (FET)" and the "spin qubit" [5, 6]. In the spin FET, the drain and source of a conventional FET are ferromagnetic. If the two ferromagnets are aligned, a spin-polarized current will behave like a normal FET current. If the ferromagnets are anti-aligned the transistor will be shut off. This could be done dynamically, allowing microprocessors to reconfigure hardware during run time. In a "spin qubit", the electron spin is used as a "quantum bit", i.e., a bit that can exist as a superposition of a pure "0" and a pure "1". Electron spins are natural "qubits" because any electron spin state is always a superposition of a spin up ("1") and a spin down ("0") state.

A major hindrance for the practical implementation of the above devices is that they require efficient spin-polarized carrier injection and transport. Conventional ferromagnetic metals are often incompatible with existing semiconductor technology. Moreover, the spin injection efficiency is often very low due to resistivity differences and to the formation of Schottky barriers [3]. *Dilute magnetic semiconductors* (DMS) may offer a solution to this problem. DMS are alloys where a stoichiometric fraction of the constituent atoms has been replaced by magnetic transition metal atoms. Such alloys are semiconducting,

[*] Corresponding author: e-mail: jrc@ices.utexas.edu, Phone: +1 512 471 3312, Fax: +1 512 471 8694

WILEY InterScience DISCOVER SOMETHING GREAT

© 2006 WILEY-VCH Verlag GmbH & Co. KGaA, Weinheim

but can possess well-defined magnetic properties (e.g., paramagnetic, anti-ferromagnetic, ferromagnetic) that conventional semiconductors do not have [7–9]. They can potentially serve as a means to inject electrons with a well defined spin and to control such spin properties in adjacent non-magnetic semiconducting layers.

It is often highly desirable to fabricate heterostructures with atomically abrupt interfaces and homogeneous compounds with precisely controlled stoichiometry. Such materials are typically unstable from any thermodynamic equilibrium considerations, but can be synthesized using non-equilibrium growth techniques such as molecular beam epitaxy. Recent studies of thin film epitaxy have led to a wealth of conceptual advances in non-equilibrium growth. One compelling example is the discovery of "surfactant action" in heteroepitaxy (A- on -B epitaxial growth), referring to the phenomenon that a low dose of a third element C serving as surface active agent (the surfactant) on the substrate B can drastically modify the growth mode of A [10, 11]. As a new layer of atoms is deposited onto the surfactant-covered substrate, the surfactant atoms keep floating at the growth front while promoting layer-by-layer growth to a thickness much larger than what would be achievable without the surfactant.

Progress in the fundamental understanding of non-equilibrium growth has in turn enabled important discoveries of novel classes of materials with intriguing physical properties. DMS are one such example [12, 13]. In these materials, when magnetic dopants such as Mn are incorporated by MBE into a semiconductor such as GaAs at concentrations greatly exceeding the thermodynamic solubility limit, the ferromagnetic ordering temperature can be significantly enhanced [12]. More recently, ferromagnetic ordering has also been observed in Mn_xGe_{1-x}, offering a better opportunity for integrating magnetism with existing silicon technology [13]. To date, the precise microscopic mechanism for ferromagnetic ordering in DMS remains an active subject of research [14–17]. Efforts to explore various possible ordering mechanisms will undoubtedly benefit from a detailed knowledge of the magnetic dopant distribution and dopant diffusion in the semiconductors. In particular, the ordering temperature, T_C, may depend sensitively on the relative populations of interstitial and substitutional dopants, as emphasized recently for DMS based on III–V semiconductors [17–19]. In order to tune the relative populations of the dopants for higher T_C, it is imperative to know the energetic and kinetic characteristics of the newly deposited dopants at the growth front.

It is known that quantum confinement of carriers greatly alters various bulk optical properties. It follows that confinement will significantly alter other properties, e.g., it will enhance spin-spin interactions in nanocrystals and change the mechanism by which magnetic interactions occur [7–9, 20]. These interactions could be exploited in future device designs based on DMS nano-crystals.

Spin-polarized electronic structure and the distribution of the magnetic moment, which are crucial for spintronics, are difficult to access experimentally. For example, doped nano-crystals are often of lower quality than the bulk material. The high temperature chemical reactions used for obtaining good quality nano-crystals may cause the Mn to segregate to the surface. Some workers have recently reported the successful growth of high quality ZnSe:Mn where the Mn does not segregate to the surface [21]. Other workers have had less success [22–25], for reasons that appear problematic. For example, Mn can be incorporated into nanocrystals of CdS and ZnSe [21, 24, 26]. In contrast, Mn cannot be incorporated into CdSe [27] even though the bulk solubilities of Mn in CdSe are close to 50%. This should not be surprising as "bulk phase" diagrams are not expected to be applicable to "nano phases," where surface free energies can become dominant. Often the term "self-purification" is used to describe the absence of defects in materials at the nanoscale [28]. There is indirect evidence for this type of mechanism. Nanoparticles of II–VI materials such as CdSe are known to undergo structural transformations from wurtzite to rocksalt at pressures removed from the bulk phase transition [29]. In particular, the pressure required for a structural transformation can be elevated by a factor of two or more. This elevated transition pressure may be explained by defects migrating from the interior of the nanocrystal to the surface. For example, dislocations may move to the surface and create steps, resulting in a nanocrystal free of nucleation sites save at the surface. In this case, the structural transformation, which cannot be initiated within the nanocrystal, occurs only at pressures higher than one observed in the bulk [30]. These transformations are also accompanied by a large hysteresis. One might expect a similar situation for point defects or

© 2006 WILEY-VCH Verlag GmbH & Co. KGaA, Weinheim

impurities, which could easily migrate a short distance. Moreover, it has been proposed that the energy of defect formation becomes less favorable as the size of the nanocrystal decreases [31]. Other theoretical models, which are also based on kinetic models involving the bonding to different surface facets, have been proposed in the Ref. [28].

In addition to experimental issues with these materials, the electronic structure of DMS *nanocrystals* has yet to be elucidated theoretically. The *ab initio* theory of bulk DMS has been rapidly evolving in recent years and has already produced numerous insights into their properties [32–37]. However, *ab initio* studies of *nanocrystals*, where at least hundreds of atoms need to be considered explicitly, are much more challenging computationally and have yet to be performed. Such studies are essential if one hopes to obtain a detailed, quantitative comprehension of size and composition effects in controlling the electronic structure and the magnetic order for device applications.

The goal of any spin electronics application is to utilize the electrons spin, in addition to its charge [1]. Such applications may include DMS materials to form an interface between magnetic and non-magnetic semiconductors, but one also needs a well-defined source of spin-polarized electrons, i.e., a ferromagnetic electrode that can be used as a source of polarized electrons. For many device applications, high values of the spin polarization at the Fermi level, provide significant benefits, e.g., large tunneling magnetoresistance [38–41] and "Ohmic" spin injection [42, 43] into semiconductors [44]. This situation has stimulated extensive efforts to find materials, the so-called *half-metallic ferromagnets*, with a polarization of 100% [1, 45]. Research within this area has generally followed a *modus operandi* of using theoretical band structures in conjunction with experimental investigations to assess promising candidates for half-metal ferromagnets. Notable successes with this line of research have been achieved, including the establishment of near 100% polarized sources for CrO_2 [46–49], completely polarized sources at low T in $La_{1-x}Sr_xMnO_3$ [50, 51], and up to 80% polarization in Fe_3O_4 [40, 52, 53]. Ideally, half metal ferromagnets should be highly polarizable and tunable, allowing for a characterization of device parameters as a function of the polarization of the electrodes.

In this brief review, we will illustrate how theoretical methods can be used to examine DMS at the bulk and nano regimes, the growth of DMS materials and a how a polarized material source can be obtained.

2 Methods for predicting the properties of spintronic materials

We use pseudopotentials constructed within density functional theory to describe the electronic and magnetic properties of spintronic materials. The pseudopotential model of condensed matter has led the way in providing a workable model for density functional theory, and modern computers have provided the computational resources to allow the implementation of this method [58, 59]. For example, it is now possible to predict accurately the properties of complex systems such as quantum dots or semiconductor liquids with thousands of atoms. The pseudopotential model treats matter as a sea of valence electrons moving in a background of ion cores. The cores are composed of nuclei and inert inner electrons. Within this model many of the complexities of an all-electron calculation are avoided. A group IV solid such as C with 6 electrons is treated in a similar fashion to Pb with 82 electrons since both have 4 valence electrons.

Within density functional theory, the many-body Schrödinger equation may be cast in terms of the *Kohn-Sham equation*:

$$\left[\frac{-\hbar^2\nabla^2}{2m} + V_{\text{tot}}[\rho(r),r]\right]\psi_i(r) = E_i\psi_i(r)\,, \tag{1}$$

where $\hbar$ is Planck's constant, m is the electron mass, and V_{tot} is the total potential at some point r in the system. The potential depends on a specific charge density $\rho(r)$, which in turn depends on the wave functions ψ_i. The problem then can be viewed as a nonlinear eigenvalue problem because of the dependence of the Hamiltonian operator on the eigenfunctions.

 © 2006 WILEY-VCH Verlag GmbH & Co. KGaA, Weinheim

physica status solidi b

With the *local density approximation* theory [60] and the use of pseudopotentials, the potential V_{tot} can be expressed as a sum of three distinct terms, specifically,

$$V_{\text{tot}} = V_{\text{ion}} + V_{\text{H}} + V_{\text{xc}} \,, \tag{2}$$

where V_{ion} is the ionic pseudopotential, V_{H} is the Hartree potential, and V_{xc} is the exchange-correlation potential. Once the charge density $\rho(r)$ is known, the Hartree potential is obtained by solving the Poisson equation:

$$\nabla^2 V_{\text{H}} = 4e\pi\rho(r) \,. \tag{3}$$

Once the charge density $\rho(r)$ is available, this can be solved by the Conjugate Gradient method or by a fast Poisson solver. This charge density is computed from the eigenfunctions ψ_i associated with the occupied states:

$$\rho(r) = -e\sum_i |\psi_i(r)|^2 \,. \tag{4}$$

Both potentials V_{H} and V_{xc} have a local character and in the finite difference scheme of discretization, they are represented by diagonal matrices. The ionic pseudopotential is more complex, consisting of both a local and a non-local term [61].

Because the total potential and the wave functions are coupled through the charge density, Eqs. (1)–(4) constitute a set of non-linear equations. These are typically solved by an inexact Newton-type method referred to as self consistent field iteration.

Once the spatial and energetic distributions of the electrons are know, the *total electronic energy*, E_{ot} of the system can be written as

$$E_{\text{tot}} = T[\rho] + E_{\text{e-i}}(\{\boldsymbol{R}_{\text{a}}\},[\rho]) + E_{\text{H}}[\rho] + E_{\text{xc}}[\rho] + E_{\text{i-i}}(\{\boldsymbol{R}_{\text{a}}\}) \,, \tag{5}$$

where $\{\boldsymbol{R}_{\text{a}}\}$ label the atomic positions, $T[\rho]$ is the kinetic energy, $E_{\text{e-i}}(\{\boldsymbol{R}_{\text{a}}\},[\rho])$ is the ionic potential energy, $E_{\text{H}}[\rho]$ is the Hartree potential energy, $E_{\text{xc}}[\rho]$ is the exchange-correlation energy, $E_{\text{i-i}}$ is the inter-ionic core interaction energy [60, 61]. The total electronic energy as a function of atomic positions can be used to compute interatomic forces without resort to classical potentials or experiment. For magnetic systems, one can consider a spin dependent version of the local density approximation [60]. In this case, the functional is written as $V_{\text{xc}} = V_{\text{xc}}[\rho_\uparrow, \rho_\downarrow]$ as the charge density is decomposed into up and down spin states [62].

There are several ways of solving for the eigenpairs of the Kohn–Sham equation. Historically, a plane wave basis has been used, especially for crystalline materials. There exist a number of "standard" codes in the literature such as `VASP` [63].

An alternative method is to solve the Kohn–Sham problem in *real space*. In this method, no explicit basis is utilized. Rather the problem is solved a grid, usually taken to be uniform. The Laplacian operator is often expressed by taking sums and differences over neighboring grid points, i.e., using a higher order finite difference method [64, 65]. This method well suited for localized systems such as quantum dots and clusters, although it can also be used for periodic systems.

3 Modeling the growth of Mn on semiconductor substrates

It imperative to know the energetic and kinetic characteristics of the newly deposited dopants at the growth front. Here we review a comparative study of the energetics and kinetics involved in Mn growth on Ge along the [100] and [111] orientations, using extensive total energy calculations within density functional theory [60]. The key findings of Zhu et al. [66] are intriguing both from the point of view of fundamental growth science and for improved understanding of the system as a DMS.

We demonstrate for the [100] orientation, the growth of Mn proceeds in a subsurface mode, i.e., the is characterized by Mn atoms having easy access to, and strong preference for, interstitial sites located

© 2006 WILEY-VCH Verlag GmbH & Co. KGaA, Weinheim

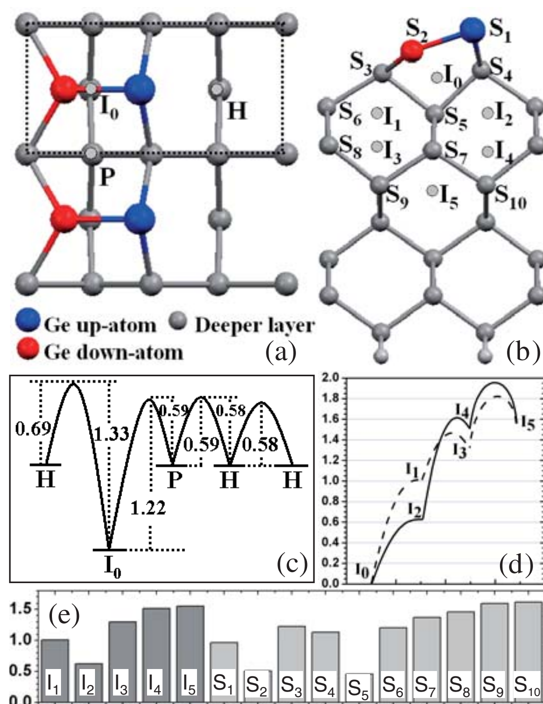

Fig. 1 (online colour at: www.pss-b.com) (a) Top view of the Ge(100)-2 × 1 surface showing the three different adsorption sites for Mn adatoms: hollow site (*H*), pedestal site (*P*) and interstitial site (I_0). (b) Side view of the Ge(100)-2 × 1 surface geometry showing the various interstitial and substitutional sites. (c) Diffusion barriers for a Mn adatom on Ge(100)-2 × 1 surface. (d) Diffusion barriers between interstitial sites beneath the Ge(100)-2 × 1 surface. (e) Total energies of interstitial and substitutional sites relative to that of I0. All the energies are in eV.

between the two topmost Ge layers. Strikingly, such a "subsurfactant action" is preserved even during epitaxial growth of additional Ge capping layers, as shown by the existence of easy kinetic pathways for the dopants trapped in deeper layers to float toward the subsurface sites. In contrast, during growth along the [111] orientation, Mn can easily diffuse into the bulk via interstitial sites. The importance of these findings can be discussed within the context of dopant control via growth manipulation and post annealing in DMS.

The spin-polarized density functional results depicted here are based on the Perdew–Wang 1991 version of the generalized gradient approximation [62] and were obtained using VASP [63]. Computational details can be found elsewhere [66].

In order to calculate adsorption and diffusion properties of a Mn adatom on the Ge(100)-2 × 1 a "supercell" geometry is employed. The structural configuration consisted of a reconstructed surface with asymmetric dimers with a 4 × 4 supercell containing eight layers of bulk Ge, a surface layer with the asymmetric dimer reconstruction, and a 13 Å-wide vacuum gap. The two layers at the bottom of the slab are fixed to their bulk positions, with all other layers fully relaxed. The bottom layer is passivated with H atoms. The geometry of this configuration is illustrated in Fig. 1.

Using such a geometry, one can extract the Mn binding energies and diffusion pathways within the surface layer. The most stable adsorption site for a Mn adatom on a (100)-2 × 1 surface is the interstitial site, I_0, located 2.2 Å beneath the Ge dimer with an absolute binding energy of 3.03 eV. The "absolute binding energy" is defined as the energy required to separate a single Mn atom from the Ge surface. The asymmetric dimer becomes almost symmetric when a Mn adatom is placed at this interstitial site. The other local metastable adsorption sites are hollow sites *H* and pedestal sites *P*, as shown in Fig. 1. The total energies of the system for a Mn adatom adsorbed at *H* and at *P* are 0.64 and 0.63 eV higher than that of the interstitial site, respectively. Unlike the case of the GaAs(100) surface [19], the substitutional site above the surface dimer is not even a metastable site, and a Mn adatom located above the dimer row can move into the pedestal site with essentially no energy barrier. Calculations of the diffusion barriers for a Mn adatom on the Ge(100)-2 × 1 surface show that the Mn adatom at the pedestal site *P* can slide into the subsurface interstitial site I_0 by overcoming an energy barrier of 0.59 eV, whereas the activation

 © 2006 WILEY-VCH Verlag GmbH & Co. KGaA, Weinheim

energy of the reverse process is 1.22 eV. These and other activation energies shown in Fig. 1 indicate that Mn diffuses relatively easily among the H and P sites, but once it dives into a subsurface interstitial site I_0 from either H or P, it will be much harder for it to hop out. The site energies and diffusion pathways of Mn in deeper layers are also shown in Fig. 1. When a Mn atom dives deeper into the bulk, the system becomes less stable. The barriers for interstitial diffusion of Mn atoms are also illustrated in Fig. 1. There is a very clear tendency for deeper Mn atoms to float toward the subsurface interstitial site I_0: For example, the pathway $I_5 \rightarrow I_3 \rightarrow I_1 \rightarrow I_0$ involves a highest activation energy of only 0.27 eV, while the pathway $I_5 \rightarrow I_4 \rightarrow I_2 \rightarrow I_0$ involves a highest activation energy of only 0.37 eV. The other potentially stable sites for a Mn atom are the substitutional sites where the Mn atom substitutes a Ge atom.

One can estimate the relative stability of Mn in interstitial sites and substitutional sites by introducing μ_{Ge}, the chemical potential of Ge, which corresponds to the total energy of a Ge atom in bulk Ge. All of the substitutional sites shown in Fig. 1 are less stable than the interstitial site I_0. In contrast, the Mn atom prefers to be substitutional in bulk Ge by as much as 0.41 eV, according to bulk calculations.

In order to substitute a Ge atom, the Mn atom must displace a Ge atom to a neighboring interstitial site. To estimate the energy cost of this process, we put the Mn atom at the S_5 site, as an example, which is the most stable substitutional site in our calculations. The S_5 Ge atom is displaced toward the neighboring interstitial sites I_0, I_1, I_2, I_3 and I_4, respectively. The total energies of these configurations are at least 1.1 eV higher than that of the configuration where the Mn atom resides at I_0. The activation energy of this process should be even higher.

The results can be summarized as follows. On a (100) surface environment, Mn strongly prefers the I_0 interstitial site. The diffusion kinetics indicates that Mn should diffuse toward I_0, regardless of whether Mn originates from the gas phase above the surface or from the bulk. Even though the substitutional site is favored inside the bulk, the kinetic barrier for substitutional incorporation is too high. As such, low temperature MBE of Mn-doped Ge(100) DMS should result in a high density of interstitial Mn atoms. As Mn atoms are buried beneath a newly deposited Ge layer, they tend to float upward toward the I_0 sites.

One can also examine the behavior of Mn on other surfaces such as Mn growth on Ge(111). The surface of Ge(111) at room temperature exhibits a $c(2 \times 8)$ reconstruction, in which each Ge adatom saturates three surface dangling bonds, while one-quarter of the surface dangling bonds remains uncovered. The equilibrium $c(2 \times 8)$ periodicity is made up of 2×2 and $c(2 \times 4)$ subunits, each of which contains one Ge adatom and one Ge rest atom. Ge adatoms reside at the T_4 site, which is located directly above an atom belonging to the lower half of the surface bilayer. This geometry is illustrated in Fig. 2.

Calculations for the adsorption energies and diffusion barriers on the $c(2 \times 8)$ surface, employed a large supercell, corresponding to two primitive $c(2 \times 8)$ unit cells, and consisting of six layers with 16 Ge atoms each. Four Ge adatoms are placed at the T_4 sites of the top surface. Sixteen hydrogen atoms passivate the bottom layer of the slab. Consecutive slabs are separated by an empty space of 13 Å wide. Atoms of the bottom two Ge layers are fixed at the corresponding bulk positions, while the other atoms are fully relaxed.

The adsorption sites and binding energies of a Mn adatom on the Ge(111)-$c(2 \times 8)$ surface relative to the configuration where the Mn is isolated far away from the surface are illustrated in Fig. 2. The H_3 sites are energetically more favorable than the T_4 sites, a prediction confirmed experimentally [67]. Among the eight H_3 sites within a primitive $c(2 \times 8)$, each of the five ($H_3^1, H_3^2, H_3^3, H_3^4, H_3^5$) has one neighboring Ge adatom and one neighboring Ge rest atom. These are the most favorable adsorption sites. Their energy differences are within 0.03 eV. The binding energy of a Mn adatom at any of the remaining H_3 sites (H_3^6, H_3^7, H_3^8) is lower by approximately 0.16 eV. The T_4 sites have approximately 0.5 eV lower binding energy compared to the most stable H_3 sites. The activation energies for Mn hopping from H_3 to T_4 sites ranges from 0.5 to 0.6 eV, while the activation energy for the reverse processes range from 0.1 to 0.3 eV.

We have also calculated the energies of the interstitial and substitutional sites in deeper layers along the [111] orientation. The total energies relative to the most stable adsorption site H_3^2 are shown in

© 2006 WILEY-VCH Verlag GmbH & Co. KGaA, Weinheim

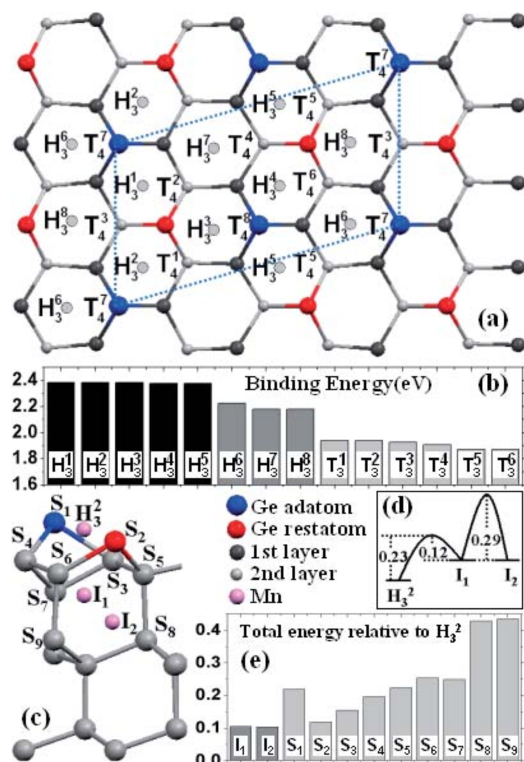

Fig. 2 (online colour at: www.pss-b.com) (a) Top view of the Ge(111)-$c(2 \times 8)$ surface indicating the various adsorption sites for a Mn adatom. (b) Binding energy of a Mn adatom at different sites on the Ge(111)-$c(2 \times 8)$. (c) Side view of the Ge(111)-$c(2 \times 8)$ surface showing the various interstitial and substitutional sites. (d) Energy barriers for Mn diffusion between the interstitial sites on Ge(111)-$c(2 \times 8)$. (e) Total energies of the interstitial and substitutional sites relative to that of the H_3^2 site. All the energies are in eV.

Fig. 2. In contrast to the case along the [100] orientation, the binding energies of the interstitial sites in deeper layers are lower than that of the H_3^2 surface site, but by only 0.11 eV. Additionally, the diffusion barrier for a Mn adatom from the H_3^2 site to the I_1 site is 0.23 eV, and the activation energy for the reverse process is 0.12 eV. The activation energy for diffusion between I_1 and I_2 is 0.29 eV, as shown in Fig. 2.

The physical origin for the contrasting behavior of Mn along the two different orientations is tied to the relative openness of the two surfaces and to the corresponding strain built near the surface regions owing to the different surface reconstructions. In particular, our calculations show that when the dimerization of the Ge atoms on the (100) surface is lifted by saturating the Ge dangling bonds with hydrogen, the stable I_0 sites become energetically unstable relative to interstitial sites that are located in deeper layers. Our results are supported by some existing experiments [68, 69], in particular, by an X-ray photoelectron spectroscopy study of MBE growth of Mn_xGe_{1-x} obtained by co-deposition of Mn and Ge on Ge(100)-2 × 1 in ultrahigh vacuum [70]. A dramatic increase of the magnetic ordering temperature, upon annealing, is accompanied by a significant increase in Mn concentration near the surface layers, an observation consistent with the results shown here [66].

The theoretical results illustrated here have important implications for experimental studies of Mn_xGe_{1-x} as a DMS for spintronic applications. (i) The high preference of Mn to the subsurface sites along the [100] orientation as predicted here should offer a natural pathway for formation of a high-density layer of Mn embedded into Ge, whose magnetic properties remain to be explored. (ii) For a Mn_xGe_{1-x} DMS system obtained by co-deposition of Ge and Mn, a high concentration of Mn will be trapped at interstitial sites in the bulk. If the system is initially grown along the [100] orientation, proper *in situ* annealing after growth should drive a significant percentage of the interstitial Mn atoms in the bulk toward the subsurface interstitial sites, thereby altering the relative populations of the Mn in substitutional and interstitial sites in the bulk. Such a population change may cause an increase of the magnetic ordering temperature, as in III–V DMS materials [71, 72] and, most recently, also in Mn_xGe_{1-x} DMS

 © 2006 WILEY-VCH Verlag GmbH & Co. KGaA, Weinheim

[70]. (iii) The orientation dependence of the Mn distribution under otherwise identical growth conditions should be readily observable. (iv) Similar subsurfactant action may be expected in other related systems [71–73].

In this section, we illustrated how pseudopotentials coupled to spin-polarized density functional calculations can be used to map out important lattice locations and diffusion barriers for Mn atoms at the growth fronts along two different surface orientations of Ge. A novel subsurface growth phenomenon termed as subsurfactant action has been predicted in MBE growth on the Ge(100)-2 × 1 surface. Mn adatoms originating from the gas phase or from deeper layers in the substrate can easily diffuse toward the interstitial sites right beneath the dimers of the Ge(100)-2 × 1 surface reconstruction where they become trapped (the I_0 sites). As Mn atoms are buried beneath a newly deposited Ge layer, they tend to move upward toward the new I_0 sites. In contrast, no subsurfactant phenomenon has been identified for Mn growth on Ge(111), where the Mn atoms can diffuse into deeper layers with relatively low energy barriers.

4 Dilute magnetic semiconductor nanocrystals

In this section, we illustrate calculations for the electronic structure and magnetic properties of Mn-containing Ge, GaAs, and ZnSe nanoparticles. This choice of semiconducting materials is motivated by several considerations. All three are well-known semiconductors, which are prototypical of group IV, III–V, and II–VI semiconductors. The elements comprising these semiconductors are found in the same row of the periodic table and these semiconductors have the same (zincblende/diamond) crystalline structure, making an identification of chemical trends easier. Also, Mn-based bulk DMS have been successfully synthesized in all three cases [74–76], and a successful synthesis of high-quality Mn-containing ZnSe nanocrystals has been reported [21].

We consider undoped nanocrystals, which were constructed by taking spherical fragments of the corresponding bulk material. The Ge surface was passivated using hydrogens, whereas the surfaces of GaAs and ZnSe were passivated using fictitious, hydrogen-like atoms with fractional charge [77]. Because magnetic circular dichroism experiments have suggested that each nanocrystal contains, on average, one Mn atom [21], the effects of placing one or two Mn atoms inside the crystal were investigated. A four-fold coordinated Mn atom was placed in the center of the Ge nanocrystal. In GaAs and ZnSe, the Mn atom was substituted on a cation site in the center of the nanocrystal. Here we will show results for four Mn-doped nanocrystals: $X_9\mathrm{Mn}Y_{10}$, $X_{18}\mathrm{Mn}Y_{19}$, $X_{40}\mathrm{Mn}Y_{41}$, and $X_{64}\mathrm{Mn}Y_{65}$, where X = Ge, Ga, or Zn and Y = Ge, As, or Se, respectively. The passivation atoms are implicit. These cases correspond to an effective Mn concentrations of 5%, 2.63%, 1.22%, and 0.77%, respectively. We will also elucidate Mn–Mn interactions by considering two Mn atoms, which were placed such that they were bridged by an anion atom. In the case of the Ge nanocrystal, we will illustrate the case for a nearest-neighbor Mn dimer.

Calculations in this section utilized a *real space* code PARSEC [78] using pseudopotentials [79] constructed from density functional theory, i.e. from the local spin density approximation [60]. The Kohn–Sham equations were solved directly on a grid using a higher-order finite difference method. Real space methods are especially efficacious for localized systems [78]. Computational details are presented elsewhere [20].

Figure 3 shows the total valence charge density ($\rho_\uparrow + \rho_\downarrow$) and spin density ($\rho_\uparrow - \rho_\downarrow$) contour plots for the 82-atom nanocrystal containing one Mn atom. In all cases studied, the charge density maps clearly show Mn bonding with its nearest neighbors, indicating Mn d-anion s–p hybridization. The spin density maps indicate a strongly localized magnetic moment at the Mn site. For the Ge and GaAs nanocrystals, the spin polarization of the atoms nearest to the Mn atom has an opposite sign to that of Mn. The spin density distribution along the Mn–As or Mn–Ge bond shows a *p* character. Its opposite spin sign is a signature of an antiferromagnetic coupling between the Mn atom and surrounding charge carriers.

© 2006 WILEY-VCH Verlag GmbH & Co. KGaA, Weinheim

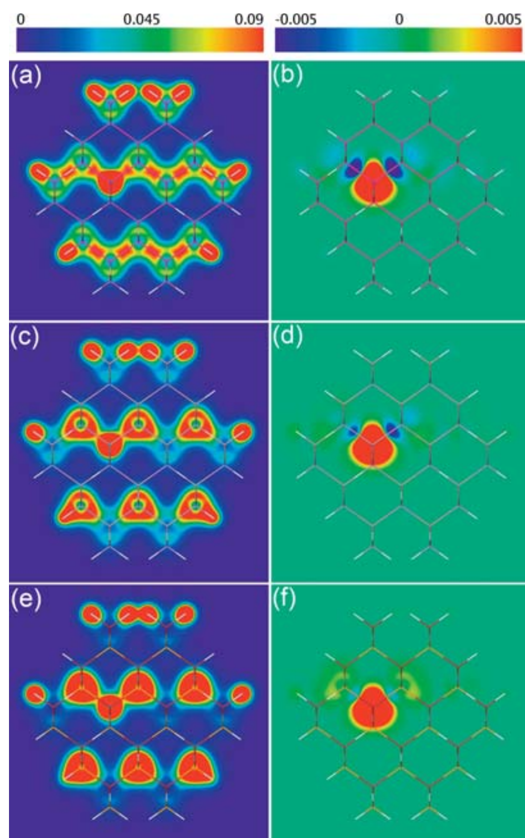

Fig. 3 (online colour at: www.pss-b.com) Total valence charge density (a), (c), (e) and spin density (b), (d), (f) for passivated $Ge_{81}Mn$, $Ga_{40}MnAs_{41}$, and $Zn_{40}MnSe_{41}$ nanocrystals.

Figure 4 shows the spin-polarized energy levels for the 82-atom system. In all three cases, the gap states are derived from Mn 3d states and reflect the splitting of the 3d states by the T_d crystal field to an e doublet and a t_2 triplet. An analysis of the corresponding wave functions shows that the valence band edge is comprised mainly of anion p states. The majority spin e levels are fully occupied, hybridized with anion p states, and located right below (~0.05 eV) the valence band edge in all three materials. The majority t_2 levels are characterized by a certain amount of hybridization with the four neighboring p orbitals and the corresponding charge density is highly localized on the MnY_4 complex.

As expected for T_d symmetry [80], the e levels have a lower energy than the t_2 levels in both spin channels. The order of the impurity related energy levels for all three systems is $e(\uparrow) < t_2(\uparrow) < e(\downarrow) < t_2(\downarrow)$. The crystal field splitting is more pronounced in the majority spin than in the minority spin and is stronger in Ge than in the polar semiconductors.

Calculations have shown that bulk Ge:Mn [81, 82] and GaAs:Mn [32, 36] are half-metallic, i.e., the Fermi level lies within a partially occupied band for the majority spins, but inside the forbidden gap for the minority spins. In contrast, bulk ZnSe:Mn was found to be semiconducting [83], i.e., the Fermi level was in the forbidden gap for both spin channels. Figure 4 shows that the e and t_2 minority spin levels are empty, so that the minority spin retains its semiconducting nature with the Mn impurity in all three cases. However, the highest occupied molecular orbitals t_2 level of the majority spin is partially occupied for Ge:Mn and GaAs:Mn, but it is fully occupied for ZnSe:Mn. This configuration is in agreement with a “half-metallic” nature of majority spin electrons for Ge and GaAs, and in agreement with the semiconducting nature for ZnSe.

A consequence of this electronic structure configuration is that the introduction of the Mn impurity does not change the number of minority spin *occupied* states. The introduction of the 5 Mn d electrons

 © 2006 WILEY-VCH Verlag GmbH & Co. KGaA, Weinheim

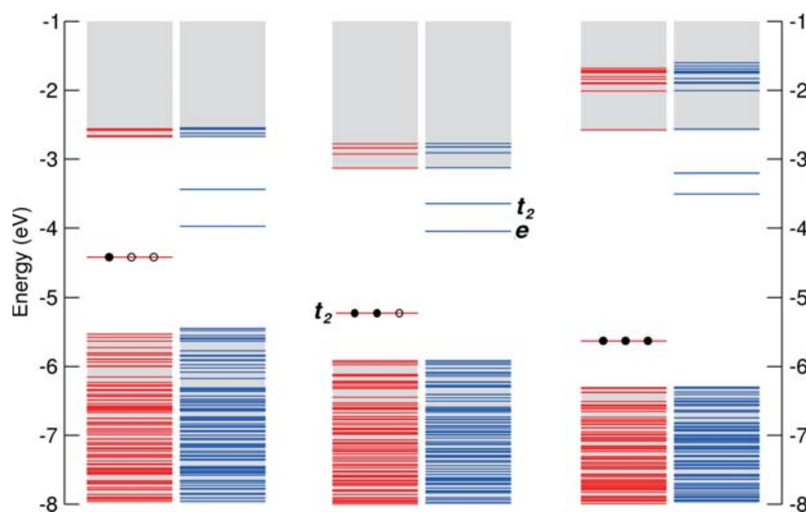

Fig. 4 (online colour at: www.pss-b.com) Spin-polarized electronic structure for passivated (a) $Ge_{81}Mn$, (b) $Ga_{40}MnAs_{41}$, and (c) $Zn_{40}MnSe_{41}$ nanocrystals. The e and t_2 levels are doubly and triply degenerate, respectively. The Fermi level is located at the majority spin t_2 levels in all cases. Filled and empty circles denote electrons and holes, respectively.

results in a net magnetic moment of $3\mu_B$, $4\mu_B$, and $5\mu_B$ for Ge, GaAs, and ZnSe, respectively. This is in agreement with the magnetic moment of $5\mu_B$ for the free Mn atom being modified by the doubly ionized acceptor, singly ionized acceptor, and isoelectronic nature of Mn in Ge, GaAs, and ZnSe, respectively. A similar picture applies to the corresponding bulk DMS [84]. Furthermore, the loss of two p electrons when Mn replaces a Ge atom but only one when it replaces a Ga atom immediately explains why the spin-polarization is more pronounced in Ge than in GaAs in the spin-density maps of Fig. 3. In principle, the partially occupied degenerate t_2 levels of the Ge:Mn and GaAs:Mn should display a Jahn–Teller effect. However, studies of bulk GaAs:Mn suggest that it is negligibly small [85].

Analysis for these nanocrystals indicates that the qualitative level splitting and magnetic moment picture is similar to that of the bulk. This is clearly a result due to the short range interaction of Mn with its neighbors. However, there remain significant differences between the electronic structure of the bulk and of the nanocrystals. These differences are due to quantum size effects, i.e., the increase of the semiconductor gap with decreasing nanocrystal size [86]. The differences are summarized in Fig. 5. We show in this figure the evolution of the "host gap" (i.e., the highest occupied molecular orbital (HOMO) – lowest unoccupied molecular orbital (LUMO) separation of states *not* derived from the Mn d orbitals), the "HOMO(host)"$\uparrow$–$t_2^{\uparrow}$ separation, and the $t_2^{\uparrow} - e^{\downarrow}$ (or ${}^4T_1 - {}^6A_1$) separation as a function of the nanocrystal diameter. It is readily observed that all three energy separations exhibit a quantum size effect; however, this effect is very pronounced for the first, less pronounced for the second, and very small for the third. This is because the Mn-related orbitals are more localized then those of the host semiconductor. The more delocalized the levels are the greater the effect of confinement. The "host gap" only involves delocalized levels and so it exhibits large energy shifts, the "HOMO(host)"$\uparrow$– $t_2^{\uparrow}$ gap involves one delocalized orbital and therefore exhibits moderate energy shifts, and the $t_2^{\uparrow} - e^{\downarrow}$ involves two localized orbitals and therefore exhibits small energy shifts.

We have chosen the $t_2^{\uparrow} - e^{\downarrow}$ as representative of transitions between localized orbitals because in ZnSe:Mn, transitions from the $e^{\downarrow}$ levels to the $t_2^{\uparrow}$ levels has been studied experimentally using photoluminescence. Its size dependence has been found to be weak [21]. Figure 5 shows that the $t_2^{\uparrow} - e^{\downarrow}$ energy separation changes from 2.25 eV to 1.81 eV as the nanocrystal size increases from 20 to 130 atoms. The experimental photoluminescence energy is expected higher (~2.1 eV Ref. [21]) than our calculated val-

© 2006 WILEY-VCH Verlag GmbH & Co. KGaA, Weinheim

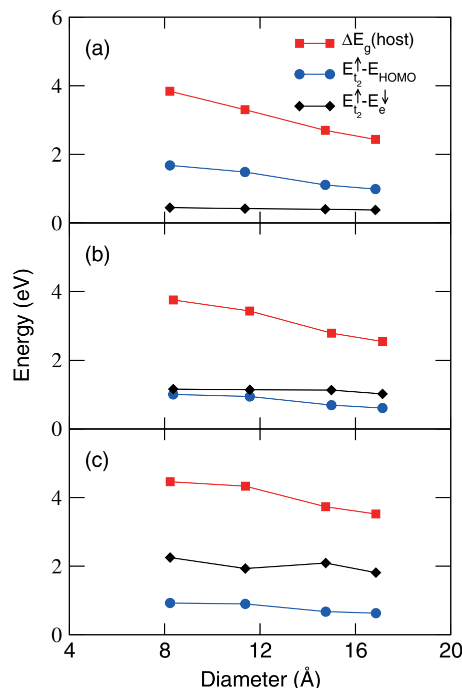

Fig. 5 (online colour at: www.pss-b.com) Energy separation of "host HOMO and LUMO" (squares), "host HOMO ↑"– $t_2^{\uparrow}$ (circles), and $t_2^{\uparrow} - e^{\downarrow}$ (diamonds) as a function of nanocrystalline diameter for (a) Ge:Mn, (b) GaAs:Mn, and (c) ZnSe:Mn.

ues. This is a well-known consequence of using the Kohn–Sham eigenvalues to predict excited state properties [87], and should not change the qualitative analysis of the size trends given here.

The strong localization of the Mn impurity levels in the MnY_4 complex implies that the choice of the Mn position within the nanocrystal should not affect its electronic structure, as long as the Mn is not close to the surface. Calculations for the 130-atom ZnSe:Mn case show an impurity level shift of less than 0.05 eV and a "host gap" change of less than 0.01 eV for different Mn positions.

The significantly different quantum size effects experienced by localized and delocalized orbitals have profound implications for the resulting electronic structure. In all cases shown in Fig. 5, the minority e and t_2 levels are well within the "host gap". In contrast, the same levels in all three corresponding bulk systems are well within the conduction band [36, 82]. The delocalized empty levels are pushed up in energy far more rapidly with decreasing size, eventually crossing the localized Mn-related levels.

A greater effect is found when examining the filled ("valence band") states of the nanocrystal. In bulk GaAs, for example, the valence band is well-known to exhibit a significant spin-splitting upon introduction of Mn [32]. No such splitting is found here, even for the 20-atom nanocrystal, where the Mn concentration is ~5%, which is comparable to bulk Mn concentrations. The significant bulk-splitting in GaAs:Mn has been attributed to the fact that Mn is a shallow acceptor [88] and can strongly interact with the valence band [33]. For the 130-atom nanocrystal, the Mn t_2 states are ~0.6 eV above the "host HOMO", because the delocalized occupied orbitals are pushed down in energy more rapidly then the Mn states with decreasing size [89]. This makes the Mn a deep acceptor, weakening the interaction and preventing spin-splitting of the occupied states. Only in the Ge:Mn nanocrystal do we see spin-splitting of the occupied states, which is consistent with the stronger Mn-host spin-interaction shown in Fig. 3.

The effect of quantum confinement on impurity-impurity spin interactions can be examined by introducing two Mn atoms into each 82-atom nanocrystal. We consider the case where both Mn atoms are placed on adjacent cation sites, bridged through an anion (in Ge one bridging Ge atom was placed between the two Mn atoms). We compared the total energy differences between the ferromagnetic or parallel spins and antiferromangetic or anti-parallel spins. The ferromagnetic structure is more stable by 0.42 eV and 0.38 eV for Ge and GaAs, respectively, but less stable by 0.14 eV for ZnSe [20]. This is in

 © 2006 WILEY-VCH Verlag GmbH & Co. KGaA, Weinheim

agreement with bulk results, where the stable phase of Ge : Mn and GaAs : Mn is predicted to be the ferromagnetic one, whereas in ZnSe : Mn the stable phase is the antiferromagnetic one. Also in agreement with bulk studies [13] is the fact that if both Mn atoms are nearest neighbors (i.e., they form a dimer) in Ge : Mn, the antiferromagnetic phase is always more stable.

In the bulk, ferromagnetism in GaAs : Mn is ascribed to a Zener-like picture of mediation by free holes [14]. Ferromagnetism in Ge:Mn has been explained either within a similar Zener-like picture [13] or within a Rudderman–Kittel–Kasuya–Yosida (RKKY) picture of interaction with free carriers [81]. However, Fig. 4 clearly shows the absence of either free holes in the valence band or a metal-like presence of free carriers, which precludes either mechanism in the present case (the electronic structure diagram of the FM nanocrystal containing two Mn atoms is qualitatively similar). We conclude that the FM interaction in nanocrystalline Ge : Mn and GaAs : Mn is *different from* that of the bulk. As noted above, the "host" valence band shifts downward rapidly compared to the Mn d states with decreasing nanocrystal size. Below some critical radius, the majority spin Mn d states appear above the top of the valence band [89]. For the size range examined here, the Mn d states form *deep* acceptors. Deep Mn impurities are known to stabilize FM interaction via a double exchange mechanism involving localized holes, as suggested previously, e.g., (Ga, Mn)N [90]. This makes the Mn-Mn interaction essentially a short-range one, consistent with the short-range spin-polarization observed in Fig. 3. Indeed, when we considered two Mn atoms separated by more than one bridging As atom, we found that: (a) such a structure was less stable than the one with a single bridging atom, (b) the energy differences between the FM and AFM phases decreased rapidly with increasing Mn-Mn separation. This suggests a novel kind of a quantum size effect – a size-dependent ferromagnetic coupling mechanism, caused by a size-dependent transition from shallow acceptors to deep acceptors.

The lack of ferromagnetism in the ZnSe : Mn nanocrystals is also consistent with the above explanation. In ZnSe : Mn, the t_2 states are fully occupied and there are no holes to couple to. In bulk ZnSe : Mn, extrinsic acceptor co-doping can be used to generate holes that can mediate the Mn–Mn spin interaction [91, 92]. To test the applicability of this idea to ZnSe : Mn nanocrystals, we replaced the bridging Se atom with a N atom in the 82-atom nanocrystal. This replacement caused the FM configuration to become lower in total energy versus the AFM configuration by 0.20 eV.

In this section, we reviewed the effect of quantum confinement on Mn-containing Ge, GaAs, and ZnSe dilute magnetic semiconductors, by means of considering the size dependence of their electronic and magnetic properties using first principles calculations. The FM and half-metallicity trends found in the bulk are preserved in the nanocrystals. However, since the Mn states are localized, they are less affected by quantum confinement than are the delocalized host states. As a consequence, in nanocrystals the Mn-related impurity states become much deeper in the gap with decreasing size. This causes the FM stabilization to be dominated by double exchange via localized holes, rather than by free holes or by an RKKY mechanism.

5 Tunable sources for spintronic materials

Ideally, fundamental studies require materials that, in addition to being highly polarized, have tunable polarization at the Fermi level, allowing for characterization of device parameters (e.g., tunneling magnetoresistance, and injection efficiency) as a function of the polarization of the electrodes. In this section, we review a simple scheme to fabricate a tunable source of spin-polarized electrons that avoids the labor-intensive surveying of candidate compounds, moving instead towards a situation where a half-metal ferromagnet can be engineered by Fermi level control.

This section centers on the pyrite structure itinerant ferromagnet CoS_2 ($T_C = 121$ K, electronic configuration: $t_{2g}^6 e_g^1$, $S = 1/2$) [54]. A recent measurement on CoS_2 yielded a polarization of 56% from point contact Andreév reflection, this measurement confirms that the pure compound is not half metallic [55]. The essential concept, which was alluded to by Zhao et al. [56] and put on a firm theoretical footing by Mazin [57], is illustrated in Fig. 6 and exploits the fact that CoS_2 has a Fermi level (E_F) that lies low in the conduction band and that it can be alloyed with FeS_2, an isostructural diamagnetic semiconductor

© 2006 WILEY-VCH Verlag GmbH & Co. KGaA, Weinheim

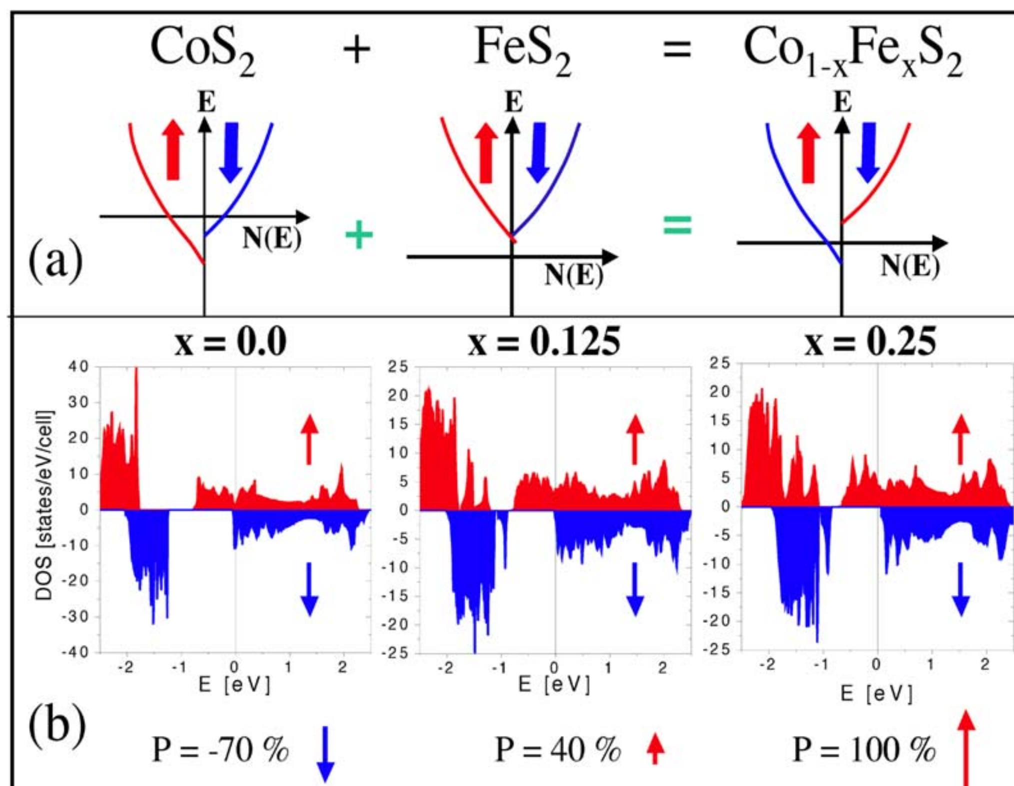

Fig. 6 (online colour at: www.pss-b.com) (a) Schematic depiction of the basic concept of composition control of EF and P in $Co_{1-x}Fe_xS_2$. (b) Calculated DOS for $x = 0$, 0.125, and 0.25. The value of the polarization at the Fermi level, P, is shown underneath the figure; E_F is taken as the zero point of energy.

($t_{2g}^6 e_g^0$, $S = 0$) [56, 57, 93, 94], with a decreased E_F. The solid solution $Co_{1-x}Fe_xS_2$ is expected to have an x dependent Fermi level, implying that in a certain composition range E_F can be decreased such that it intersects the majority spin band while lying in a gap for the minority spins, producing $P = 100\%$ [see Fig. 6].

In order to verify the essential features of this picture, electronic structure calculations have been performed. The results are presented in Fig. 6 for $x = 0$, 0.125, and 0.25. These calculations employed pseudopotentials constructed within the local-spin-density approximation [60]. Computational details are presented in the Ref. [95].

$Co_{1-x}Fe_xS_2$ solid solutions can be described by an ordered supercell approach (e.g., Co_7FeS_{16} for $x = 0.125$) using equivalent sets of k-points. The effect of disorder (i.e., random alloy versus ordered supercell) on the density of states and the saturation magnetization were addressed by Mazin [57] and found to be small. The same (experimental) crystal structure parameters were used for all alloy compositions ($a = 5.524$ Å and $u = 0.389$ for $0 < x < 0.3$ in $Co_{1-x}Fe_xS_2$) [96].

The electronic band structures for these materials are indistinguishable from that obtained previously by Shishidou et al. [97] using the full-potential linear augmented-plane-wave method in conjunction with the local spin density approximation. However, the density of state (Fig. 6) was obtained using a linear tetrahedral method of summation and exhibits some important differences from the previous work, especially in the vicinity of E_F. In contrast to that calculation, CoS_2 is a *minority* spin system, owing to the sharp feature in the minority density of states at E_F. Increasing the Fe doping component leads to the anticipated decrease in E_F. Near $x = 0.125$ the Fermi level has a small the minority spin band contribution to the density of states, and a large majority contribution. Fe doping induces an unexpected sign change

 © 2006 WILEY-VCH Verlag GmbH & Co. KGaA, Weinheim

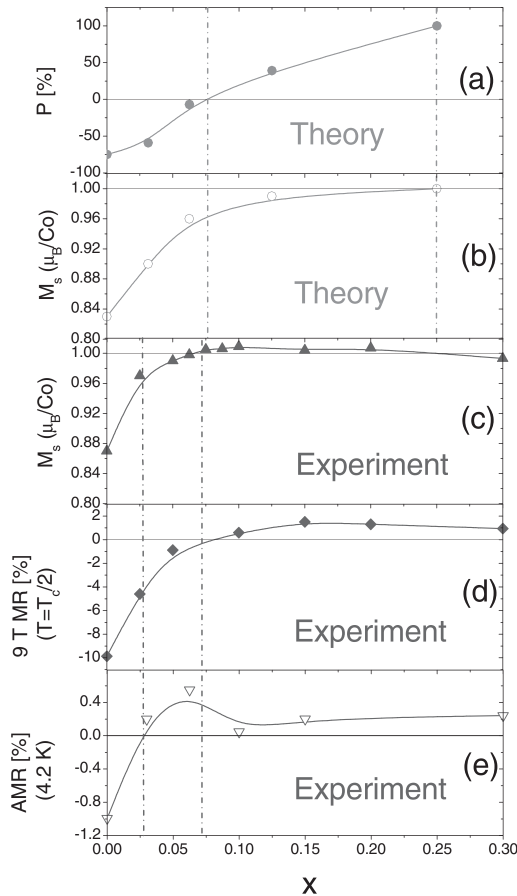

Fig. 7 (online colour at: www.pss-b.com) Composition dependence of (a) the theoretical P, (b) the predicted low temperature saturation magnetization (M_S), (c) the experimental M_S (assuming no moment on Fe), (d) the high field (9 T) magnetoresistance at $0.5T_C$, and (e) the experimental anisotropic magnetoresistance at 4.2 K. The anisotropic magnetoresistance is defined as $(\rho_\parallel - \rho_\perp)/\rho(0))$, where $\rho_\parallel$ is the resistivity measured with field parallel to current, $\rho_\perp$ is the resistivity measured with field perpendicular, and $\rho(0)$ is the zero field value. The experimental data is from Ref. [95].

in the spin polarization at the Fermi level. Further doping lowers the Fermi level into the gap for the minority spins, while maintaining a large density of states for the majority spins, yielding $P = 100\%$ at $x = 0.25$, i.e., this Fe concentration creates a half-metallic ferromagnetism.

Figure 7 shows theoretical prediction for the polarization and saturation magnetization as a function of Fe doping. As previously discussed, the theoretical polarization first reverses sign and then reaches 100% at $x = 0.25$. The corresponding theoretical for the saturation magnetization assume a non-integer value at $x = 0$ (consistent with $P < 100\%$), which increases with x reaching exactly $1\mu_B$/Co at $x = 0.25$. The experimental results reveal good agreement with the theoretical predictions. A saturation magnetization of $1\mu_B$/Co is achieved at $x = 0.07$ and is maintained up to $x = 0.30$.

Experiment is consistent with the attainment of a half metal ferromagnetic state at $x = 0.07$, although the data do not constitute direct proof. Further evidence is provided by the high field magnetoresistance, which was measured at $T = 0.5T_C$ at each x value. Consistent with $P < 100\%$, significant negative magnetoresistance is observed at $x = 0$, owing to the expected field-induced suppression of spin-flip scattering. In agreement with the magnetoresistance compositional data, $M_S(x)$, (which attains $1\mu_B$/Co at $x = 0.07$) this negative magnetoresistance vanishes at exactly $x = 0.07$, where it is replaced with a small positive contribution that peaks at T_C. The remarkable agreement between the x value for the attainment of saturation magnetization, $1\mu_B$/Co, and the vanishing of the high field magnetoresistance must be considered as strong evidence for a highly polarized state at $x = 0.07$.

The compositional dependence of the anisotropic magnetoresistance is also consistent with this scenario. The anisotropic magnetoresistance is negative for undoped CoS_2 but reverses sign at $x = 0.03$,

© 2006 WILEY-VCH Verlag GmbH & Co. KGaA, Weinheim

which one can interpret as a crossover from minority spin to majority spin behavior, as predicted by these calculations. Note that the vertical dotted lines in Fig. 7 indicate the positions of the sign reversal in polarization and the apparent attainment of $P = 100\%$.

While the experimental measurement and theoretical predictions are quite good, there are some problematic issues (see Ref. [95]). For example, the experimental values of P do not confirm an initial decrease in the polarization. Also, the measured polarization does not saturate to 100% and the observed doping levels for a reversal are not consistent with theory. There are a several plausible explanations for these difference, including the lack of disorder and surface effects in the theoretical predictions. Moreover, the experimental polarization involves a current measurement, which is not solely dependent of the density of states at the Fermi level.

6 Summary

In this review, we have illustrated three examples of how theoretical methods can be used to predict properties of spintronic materials.

We illustrated the feasibility of a simple scheme for engineering a high spin polarization at the Fermi level in $Co_{1-x}Fe_xS_2$ by varying the composition. A combination of indirect transport probes, direct measurement by point contact Andreév reflection, and electronic structure calculations provides a consistent picture, where the spin polarization can be continuously tuned in the range $56\% < P < 85\%$. Along with the close lattice match to technologically relevant materials such as Si and GaAs, this opens up the possibility of employing these materials as tunable sources of polarized electrons for fundamental studies in spin electronics.

One can also use theoretical methods to examine the role of quantum confinement in Mn-containing Ge, GaAs, and ZnSe dilute magnetic semiconductors, by considering the size dependence of their electronic and magnetic properties using first principles calculations. The ferromagnetic and half-metallicity trends found in the bulk are preserved in the nanocrystals. However, since the Mn states are localized, they are less affected by quantum confinement than are the delocalized host states. As a consequence, in nanocrystals the Mn-related impurity states become much deeper in the gap with decreasing size. This causes a ferromagnetic stabilization to be dominated by double exchange via localized holes, rather than by free holes or by an RKKY mechanism.

Finally, we reviewed how pseudopotential spin-polarized density functional calculations can be used to map out the important lattice locations and diffusion barriers for Mn atoms at the growth fronts along two different orientations of Ge. A novel subsurface growth phenomenon: “subsurfactant action” was predicted in MBE growth on the Ge(100)-2 × 1 surface. Mn adatoms originating from the gas phase or from deeper layers in the substrate can easily diffuse toward the interstitial sites right beneath the dimers of the Ge Ge(100)-2 × 1 surface reconstruction where they become trapped (the I_0 sites). As Mn atoms are buried beneath a newly deposited Ge layer, they tend to float upward toward the new I_0 sites. In contrast, no subsurfactant phenomenon has been identified for Mn growth on Ge(111), where the Mn atoms can diffuse into deeper layers with relatively low energy barriers. Several important implications of these predictions have been proposed, awaiting confirmation in future experimental studies of Mn_xGe_{1-x} as a dilute magnetic semiconductor.

Acknowledgements This work was supported in part by the National Science Foundation under DMR-0551195. Calculations were performed at the Minnesota Supercomputing Institute and at the Texas Advanced Computing Center.

References

[1] S. A. Wolf, D. D. Awschalom, R. A. Buhrman, J. M. Daughton, S. von Molnar, R. L. Roukes, A. Y. Chtchelkanova, and D. M. Treger, Science **294**, 1488 (2001).
[2] D. D. Awschalom, D. Loss, and N. Samarth (Eds.), Semiconductor Spintronics and Quantum Computation (Springer, Berlin, 2002).

 © 2006 WILEY-VCH Verlag GmbH & Co. KGaA, Weinheim

[3] P. Ball, Nature **404**, 918 (2000).
[4] D. D. Awschalom and J. M. Kikkawa, Physics Today **52**, 33 (1999).
[5] S. Datta and B. Das, Appl. Phys. Lett. **56**, 665 (1990).
[6] G. Burkard, D. Loss, and D. P. DiVincenzo, Phys. Rev. B **59**, 2070 (1999).
[7] J. K. Furdyna and J. Kossut, in: Dilute Magnetic Semiconductors, Vol. 25 of Semiconductors and Semimetals, series edited by R. K. Willardson and A. C. Beer (Academic Press, Boston, 1988).
[8] J. K. Furdyna, J. Appl. Phys. **64**, R29 (1988).
[9] M. Jain, Diluted Magnetic Semiconductors (World Scientific, Singapore, 1991).
[10] M. Copel, M. C. Reuter, E. Kaxiras, and R. M. Tromp, Phys. Rev. Lett. **63**, 632 (1989).
[11] W. F. Egelhoff and D. A. Steigerwald, J. Vac. Sci. Technol. A **7**, 2167 (1989).
[12] H. Ohno, A. Shen, F. Matsukura, A. Oiwa, A. Endo, S. Katsumoto, and Y. Iye, Appl. Phys. Lett. **69**, 363 (1996).
[13] Y. D. Park, A. T. Hanbicki, S. C. Erwin, C. S. Hellberg, J. M. Sullivan, J. E. Mattson, T. F. Ambrose, A. Wilson, G. Spanos, and B. T. Jonker, Science **295**, 651 (2002).
[14] T. Dietl, H. Ohno, F. Matsukura, J. Cibert, and D. Ferrand, Science **287**, 1019 (2000).
[15] S. Das Sharma, E. H. Hwang, and A. Kaminski, Solid State Commun. **127**, 99 (2003).
[16] T. Jungwirth, Jairo Sinova, K. Y. Wang, K. W. Edmonds, R. P. Campion, B. L. Gallagher, C. T. Foxon, Qian Niu, and A. H. MacDonald, Appl. Phys. Lett. **83**, 320 (2003).
T. Jungwirth, Jairo Sinova, J. Masek, J. Kucera, and A. H. MacDonald, Rev. Mod. Phys., in press (2006).
[17] C. Timm, J. Phys.: Condens. Matter **15**, R1865 (2003).
[18] K. M. Yu, W. Walukiewicz, T. Wojtowicz, I. Kuryliszyn, X. Liu, Y. Sasaki, and J. K. Furdyna, Phys. Rev. B **65**, 201303 (R) (2002).
[19] S. C. Erwin and A. G. Petukhov, Phys. Rev. Lett. **89**, 227201 (2002).
[20] X. Huang, A. Makmal, J. R. Chelikowsky, and L. Kronik, Phys. Rev. Lett. **94**, 236801 (2005).
[21] D. J. Norris, N. Yao, F. T. Charnock, and T. A. Kennedy, Nano Lett. **1**, 3 (2001).
[22] Y. Wang, N. Herron, K. Moller and T. Bien, Solid State Commun. **77**, 33 (1991).
[23] R. N. Bhargava, D. Gallagher, X. Hong, and A. Nurmikko, J. Phys. Chem. **100**, 18322 (1996).
[24] J. F. Suyver, S. F. Wuister, J. J. Kelly, and A. Meijerink, Phys. Chem. Chem. Phys. **2**, 5445 (2000).
[25] K. M. Hanif, R. W. Meulenberg, and G. F. Strouse, J. Am. Chem. Soc. **124**, 11495 (2002).
[26] L. Levy, J. F. Hochepied, and M. P. Pileni, J. Phys. Chem. **100**, 18322 (1996).
[27] F. V. Mikulec, M. Kuno, M. Bennati, D. A. Hall, R. G. Griffin, and M. G. Bawendi, J. Am. Chem. Soc. **122**, 2532 (2000).
[28] S. C. Erwin, L. Zu, M. I. Haftel, A. L. Efros, T. A. Kennedy, and D. J. Norris, Nature **436**, 91 (2005).
[29] S. H. Tolbert and A. P. Alivisatos, Science, 373 (1994).
J. N. Wickham, A. B. Herhold, and A. P. Alivisatos, Phys. Rev. Lett. **84**, 923 (2000).
[30] S. Limpijumnong and S. Jungthawan, Phys. Rev. B **70**, 054104 (2004).
[31] G. Dalpian and J. R. Chelikowsky, Phys. Rev. Lett. **96**, 226802 (2006).
[32] M. Jain, L. Kronik, J. R. Chelikowsky and V. V. Godlevsky, Phys. Rev. B **64**, 245205 (2001).
[33] L. Kronik, M. Jain and J. R. Chelikowsky, Phys. Rev. B **66**, 041203 (2002); Appl. Phys. Lett. **85**, 2014 (2004).
[34] G. J. Theurich and N. A. Hill, Phys. Rev. B **66**, 115208 (2002).
[35] S. Sanvito and N. A. Hill, Appl. Phys. Lett. **78**, 3493 (2001).
[36] S. Sanvito, P. Ordejon, and N. A. Hill, Phys. Rev. B **63**, 165206 (2001).
[37] M. van Schilfgaarde and O. N. Myrasov, Phys. Rev. B **63**, 233205 (2001).
[38] M. Bowen, M. Bibes, A. Barthélémy, J.-P. Contour, A. Anane, Y. Lemaître, and A. Fert, Appl. Phys. Lett. **82**, 233 (2003).
[39] G. Hu and Y. Suzuki, Phys. Rev. Lett. **89**, 276601 (2002).
[40] J. S. Parker, P. G. Ivanov, D. M. Lind, and P. Xiong, Phys. Rev. B **69**, 220413(R) (2004).
[41] A. Gupta and J. Z. Sun, J. Magn. Magn. Mater. **200**, 24 (1999).
[42] R. Fiederling, M. Keim, G. Reuscher, W. Ossau, G. Schmidt, A. Waag, and L. W. Molenkamp, Nature **402**, 787 (1999).
[43] Y. Ohno, D. K. Young, B. Beschoten, F. Matsukura, H. Ohno, and D. D. Awschalom, Nature **402**, 790 (1999).
[44] G. Schmidt, D. Ferrand, L. W. Molenkamp, A. T. Filip, and B. J. van Wees, Phys. Rev. B **62**, 4790 (R) (2000).
[45] C. M. Fang, G. A. de Wijs, and R. A. de Groot, J. Appl. Phys. **91**, 8340 (2002).
[46] K. P. Kämper, W. Schmitt, and G. Güntherodt, R. J. Gambino and R. Ruf, Phys. Rev. Lett. **59**, 2788 (1987).
[47] Y. Ji, G. J. Strijkers, F. Y. Yang, C. L. Chien, J. M. Byers, A. Anguelouch, Gang Xiao, and A. Gupta, Phys. Rev. Lett. **86**, 5585 (2001).

© 2006 WILEY-VCH Verlag GmbH & Co. KGaA, Weinheim

[48] E. J. Singley, C. P. Weber, D. N. Basov, A. Barry, and J. M. D. Coey, Phys. Rev. B **60**, 4126 (1999).
[49] J. S. Parker, S. M. Watts, P. G. Ivanov, and P. Xiong, Phys. Rev. Lett. **88**, 196601 (2002).
[50] J.-H. Park, E. Vescovo, H.-J. Kim, C. Kwon, R. Ramesh, and T. Venkatesan, Phys. Rev. Lett. **81**, 1953 (1998).
[51] B. Nadgorny, I. I. Mazin, M. Osofsky, R. J. Soulen, Jr., P. Broussard, R. M. Stroud, D. J. Singh, V. G. Harris, A. Arsenov, and Ya. Mukovskii, Phys. Rev. B **63**, 184433 (2001).
[52] Yu. S. Dedkov, U. Rüdiger, and G. Güntherodt, Phys. Rev. B **65**, 064417 (2002).
[53] S. A. Morton, G. D. Waddill, S. Kim, I. K. Schuller, S. A. Chambers, and J. G. Tobin, Surf. Sci. **513**, L451 (2002).
[54] H. Hiraka and Y. Endoh, J. Phys. Soc. Jpn. **63**, 4573 (1994).
[55] L. Wang, T. Y. Chen, and C. Leighton, Phys. Rev. B **69**, 094412 (2004).
[56] G. L. Zhao, J. Callaway, and M. Hayashibara, Phys. Rev. B **48**, 15781 (1993).
[57] I. I. Mazin, Appl. Phys. Lett. **77**, 3000 (2000).
[58] J. Bernholc, Physics Today **59**, 30 (1999).
[59] J. R. Chelikowsky and S. G. Louie, Quantum Theory of Real Materials (Kluwer Press, 1996).
[60] P. Hohenberg and W. Kohn, Phys. Rev. **136**, B864 (1964).
W. Kohn and L. Sham, Phys. Rev. **140**, A1133 (1965).
S. Lundqvist and N. H. March, Theory of the Inhomogeneous Electron Gas (Plenum, New York, 1983).
R. G. Parr and W. Yang, Density Functional Theory of Atoms and Molecules (Oxford, New York, 1989).
R. M. Dreizler and E. K. U. Gross, Density Functional Theory (Springer-Verlag, Berlin, 1990).
[61] D. R. Hamann, M. Schlüter, and C. Chiang, Phys. Rev. Lett. **43**, 1494 (1979).
G. Kerker, J. Phys. C **13**, L189 (1980).
D. Vanderbilt, Phys. Rev. B **32**, 8412 (1985).
A. Rappe, K. M. Rabe, E. Kaxiras, and J. D. Joannopoulos, Phys. Rev. B **43**, 1227 (1990).
J. R. Chelikowsky and M. L. Cohen, Ab initio Pseudopotentials for Semiconductors, in: Handbook on Semiconductors, edited by Peter Landsberg (Elsevier, Amsterdam, 1992), Vol. 1, p. 59.
[62] J. P. Perdew and Y. Wang, Phys. Rev. B **45**, 13244 (1992).
[63] G. Kresse and J. Furthmüller, Phys. Rev. B **54**, 11169 (1996).
[64] J. R. Chelikowsky, J. Phys. D **33**, R33 (2000).
J. R. Chelikowsky, Y. Saad, S.Öğüt, I. Vasiliev, and A. Stathopoulos, phys. stat. sol. (b) **217**, 173 (2000).
[65] J. R. Chelikowsky, N. Troullier, and Y. Saad, Phys. Rev. Lett. **72**, 1240 (1994).
[66] W. Zhu, H. H. Weitering, E. G. Wang, E. Kaxiras, and Z. Zhang, Phys. Rev. Lett. **93**, 126102 (2004).
[67] C. G. Zeng, W. G. Zhu, S. C. Erwin, Z. Y. Zhang, and H. H. Weitering, Phys. Rev. B **70**, 205340 (2004).
[68] F. D'Orazio, F. Lucari, M. Passacantando, P. Picozzi, S. Santucci, and A. Verna, IEEE Trans. Magn. **38**, 2856 (2002).
[69] L. Liu, N. Chen, Z. Yin, F. Yang, J. Zhou, and F. Zhang, J. Cryst. Growth **265**, 466 (2004).
[70] A. P. Li, J. F. Wendelken, J. Shen, L. C. Feldman, J. R. Thompson, and H. H. Weitering, Phys. Rev. B **72**, 195205 (2005).
[71] S. J. Potashnik, K. C. Ku, S. H. Chun, J. J. Berry, N. Samarth, and P. Schiffer, Appl. Phys. Lett. **79**, 1495 (2001).
[72] K. W. Edmonds, P. Boguslawski, K. Y. Wang, R. P. Campion, S. N. Novikov, N. R. S. Farley, B. L. Gallagher, C. T. Foxon, M. Sawicki, T. Dietl, M. Buongiorno Nardelli, and J. Bernholc, Phys. Rev. Lett. **92**, 037201 (2004).
[73] R. L. Headrick, I. K. Robinson, E. Vliek, and L. C. Feldman, Phys. Rev. Lett. **63**, 1253 (1989); P. Bedrossian, R. D. Meade, K. Mortensen, D. M. Chen, J. A. Golovchenko, and D. Vanderbilt, Phys. Rev. Lett. **63**, 1253 (1989).
I. W. Lyo, E. Kaxiras, and Ph. Avouris, Phys. Rev. Lett. **63**, 1261 (1989).
[74] S. Cho, S. Choi, S. C. Korea, Y. Kim, J. B. Ketterson, B. Kim, Y. C. Kim, and J. Jung, Phys. Rev. B **66**, 033303 (2002).
[75] H. Ohno, Science **281**, 951 (1998).
[76] B. Oczkiewicz, A. Twardowski, and M. Demianiuk, Solid State Commun. **64**, 107 (1987).
[77] X. Huang, E. Lindgren, and J. R. Chelikowsky, Phys. Rev. B **71**, 165328 (2005).
[78] J. R. Chelikowsky, N. Troullier, and Y. Saad, Phys. Rev. Lett. **72**, 1240 (1994); http://www.ices.utexas.edu/parsec.
[79] N. Troullier and J. Martins, Phys. Rev. B **43**, 1993 (1991).
[80] S. Blundell, Magnetism in Condensed Matter (Oxford University Press, New York, 2001).
[81] Y.-J. Zhao, T. Shishidou, and A. J. Freeman, Phys. Rev. Lett. **90**, 047204 (2003).
[82] A. Stroppa, S. Picozzi, A. Continenza, and A. J. Freeman, Phys. Rev. B **68**, 155203 (2003).

 © 2006 WILEY-VCH Verlag GmbH & Co. KGaA, Weinheim

[83] L. M. Sandratskii, Phys. Rev. B **68**, 224432 (2003).
[84] T. C. Schulthess and W. H. Butler, J. Appl. Phys. **89**, 7021 (2001).
[85] X. Lou and R. M. Martin, Phys. Rev. B **72**, 035212 (2005).
[86] L. Bányai and S. W. Koch, Semiconductor Quantum Dots (World Scientific Publ. Co. Pte. Ltd., Singapore, 1993), and references therein.
[87] J. R. Chelikowsky, L. Kronik, and I. Vasiliev, J. Phys.: Condens. Matter **15**, R1517 (2003).
[88] M. Linnarsson, E. Janzen, B. Monemar, M. Kleverman, and A. Thilderkvist, Phys. Rev. B **55**, 6938 (1997).
[89] S. Sapra, D. D. Sarma, S. Sanvito, and N. A. Hill, Nano Lett. **2**, 605 (2002).
[90] T. Graf, S. T. B. Goennenwein, and M. S. Brandt, phys. stat. sol. (b) **239**, 277 (2003).
K. Sato, W. Schweika, P. H. Dederichs, and H. Katayama-Yoshida, Phys. Rev. B **70**, 201202(R) (2004).
M. Wierzbowska, D. Sánchez-Portal, and S. Sanvito, Phys. Rev. B **70**, 235209 (2004).
[91] A. Haury, A. Wasiela, A. Arnoult, J. Cibert, S. Tatarenko, T. Dietl, and Y. M. d'Áubigne, Phys. Rev. Lett. **79**, 511 (1997).
[92] D. Ferrand, J. Cibert, A. Wasiela, C. Bourgognon, S. Tatarenko, G. Fishman, T. Andrearczyk, J. Jaroszynski, S. Kolesnik, T. Dietl, B. Barbara, and D. Dufeu, Phys. Rev. B **63**, 085201 (2001).
[93] S. K. Kwon, S. J. Youn, and B. I. Min, Phys. Rev. B **62**, 357 (2000).
[94] H. S. Jarrett, W. H. Cloud, R. J. Bouchard, S. R. Butler, C. G. Frederick, and J. L. Gillson, Phys. Rev. Lett. **21**, 617 (1968).
[95] L. Wang, K. Umemoto, R. M. Wentzcovitch, T. Y. Chen, C. L. Chien, J. G. Checkelsky, J. C. Eckert, E. D. Dahlberg, and C. Leighton, Phys. Rev. Lett. **94**, 056602 (2005).
[96] R. W. G. Wyckoff, Crystal Structures (Interscience, New York, 1965), Vol. 1.
[97] T. Shishidou, A. J. Freeman, and R. Asahi, Phys. Rev. B **64**, 180401 (2001).
[98] T. R. McGuire and R. I. Potter, IEEE Trans. Magn. **11**, 1018 (1975).

© 2006 WILEY-VCH Verlag GmbH & Co. KGaA, Weinheim